Accuracy evaluation of ITCsF2: a Nitrogen cooled Cesium Fountain.

Filippo Levi, Davide Calonico, Claudio E. Calosso, Aldo Godone, and Salvatore Micalizio
INRIM - Str. Delle Cacce 91, 10135 Torino, Italy
Giovanni A. Costanzo
Politecnico di Torino – Corso Duca degli Abruzzi 24, 10129 Torino, Italy.

Abstract

Since almost two decades, Cesium fountain Primary Frequency Standards (PFS) represent the best realization of the definition of the second in the International System (SI) of units. Their accuracy has progressively improved with time, reaching few parts in 10^{-16}. In this paper we present the accuracy evaluation of ITCsF2, a Cs fountain PFS developed at the Italian National Metrological Institute (INRIM), designed to be operated at cryogenic temperature to reduce the blackbody radiation shift. The short term stability of the ITCsF2 fountain is $2\times10^{-13}\tau^{-1/2}$ when operated at high atomic density and, the relative inaccuracy 2.2×10^{-16}. We also report also four calibrations of the International Atomic Time (TAI) with a relative frequency agreement of $(-1.7\pm3.2)\times10^{-16}$, between ITCsF2 and the average of the other fountains operated in the world in the reference periods.

1. Introduction

Since its discovery in the early 1980s, laser cooling of neutral atoms has attracted the attention of the time and frequency community for its possible application to the development of a new generation of Cs primary frequency standards. Indeed, the first Cs fountain [1] immediately demonstrated an accuracy better than that of thermal beams standards realized until then. In the following years, new fountains were developed in many different laboratories worldwide, improving by more than one order of magnitude the realization of the SI second [1-11].

After the first report of a fountain to the Bureau International de Poids e des Mesures (BIPM) in 1995, regular fountain evaluations have been reported since 1999, increasing then progressively their weight in TAI calibration [12] becoming quickly the fundamental stone for time and frequency accuracy worldwide; eleven fountains have reported frequency accuracy evaluations to BIPM until

today. Among other institutes, INRIM has contributed to this process since 2003, operating the Cs fountain ITCsF1 with a typical uncertainty of $1x10^{-15}$ in the realization of the SI second [6].
A remarkable work [12] has shown a substantial statistical agreement among all the fountains that have reported data to BIPM to steer the TAI.
A significant amount of theoretical and experimental work progressively improved the accuracy of the Cs fountains, properly evaluating the frequency biases in the pulsed regime, typical of these primary frequency standards. In particular several tests have been developed to produce a strong leverage effect in the assessment of several biases: magnifying the bias, those tests allowed better evaluations and reduced uncertainties [13-18]. As a result, many of the biases affecting a fountain can now be evaluated with a relative uncertainty in the 10^{-17} range.
In this paper, we present and discuss the complete accuracy evaluation of ITCsF2, the new INRIM Cs fountain ITCsF2 [19]. One of the most important peculiarity of ITCsF2 is the strong reduction of the blackbody radiation shift, achieved maintaining the interaction region of the standard at the liquid nitrogen temperature (89.4 K). ITCsF2 was operated almost continuously in the last two years, allowing a complete and repeatable accuracy budget. Several informal accuracy evaluations were performed against TAI, confirming the accuracy of the standard.
In the first part of the paper, a detailed description of ITCsF2 apparatus is given; in the second, the analysis of the frequency biases affecting the standard is presented, together with their measurement methods and uncertainty; the last part is devoted to the frequency comparisons between ITCsF2 and TAI realized so far.
IT-CsF2 has been realized in tight collaboration with NIST time and frequency division (Boulder CO), where the physical package of the fountain was designed and realized. A twin system, NIST-F2, that works at liquid nitrogen temperature as well, is operated there.

2. Description of the standard

2.1 Physical package

figure 1 shows a schematic drawing of the fountain apparatus, that is 230 cm tall. The main features of its design are related to the cryogenic temperature operation, achieved by liquid nitrogen cooling. The physical structure is composed of two parts, one kept at room temperature and the other in thermal contact with a liquid nitrogen cryostat. The cryostat is thermally insulated through a mid-vacuum (MV) chamber containing the cryostat itself, the C-field solenoid, the magnetic shields and the cavity feeding coaxial cables. The second part is an ordinary ultra high vacuum (UHV) chamber

where all the atomic manipulations and interactions are performed.

The UHV volume consists of a lower camera, that hosts the atoms trapping and the detection regions, and an upper region that includes the state selection and the Ramsey interaction cavities and the drift tube. The lower chamber is kept at room temperature, whilst the upper part is cold. The temperature difference between the two parts is maintained with a stainless steel vacuum bellow, specifically designed also to electrically insulate the two zones, avoiding thermoelectric currents flow.

The trapping and the detection chamber is provided with six recesses for the collimators of the molasses beams oriented according to the (1,1,1) geometry; given the mechanical design, minimum tilt adjustment is required to properly align the trapping beams. Micrometric screws allow a fine adjustment of the beams. The collimators, shown in figure 2, use the natural divergence of the fiber output, and a single plano-convex lens to generate a collimated Gaussian beam of 25 mm diameter (at 1/e). Polarization optics are placed inside each collimator to improve the quality of the beams and to reduce the cross talk between each couple of counter-propagating beams in the power control system described in a following section.

A first polarizing beam splitter cube cleans the polarization noise introduced by the PM-fiber, then a pick-off optics sends a fraction of the beam to a large area photodiode, that is used to stabilize and control the laser beam power during the fountain cycle. A linear film polarizer (absorber) is then placed along the beam to minimize the counter-propagating beam light impinging the detector used in the laser power control loop.

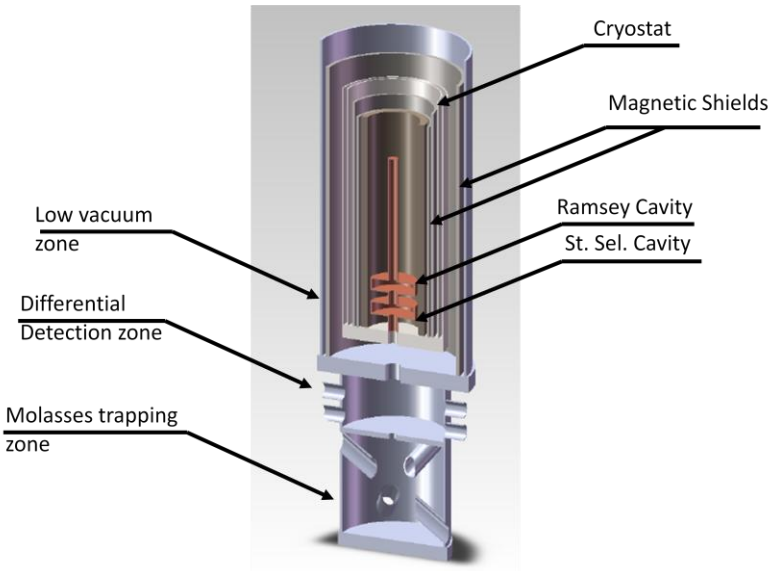

Figure 1. Schematic drawing of ITCsF2 physical package.

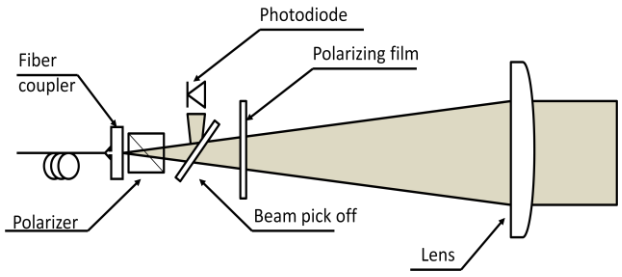

Figure 2. Schematic of the laser collimators.

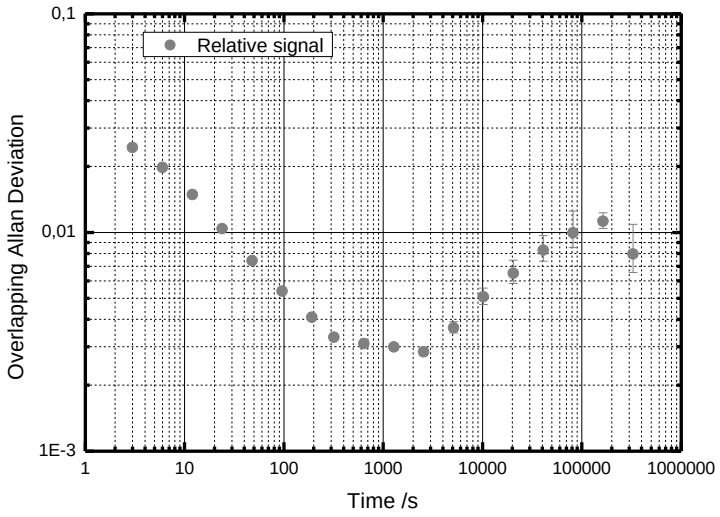

Figure 3. Stability of the Time Of Flight signal from the detection.

Figure 3 shows the relative stability of the detected time-of-flight (TOF). The shot-to-shot atom number stability is always lower than 3% and in the long-term, up to several days, a stability better than 1% is achieved. To reach this signal stability, the power of the detection beams is electronically stabilized with a servo system similar to that of the trapping beams.

A fixed collimator is used to deliver the repumper light into the trapping chamber; no power servo is used in this case.

The Cs oven consists of a simple copper tube, where a Cs ampoule is located. After the bake-out of the system the ampoule is broken, and the cesium vapor released. The oven temperature is controlled with Peltier elements and it is set around 23°C.

A steel plate separates the lower part of the trapping chamber from the upper detection region.

Graphite getters are placed in the trapping zone to reduce the Cs vapor diffusion into the detection region.

Similarly to the design of IT-CsF1 [20] the detection zone is twofold, allowing for spatially well separate detection of atoms in the F=4 ground state and in the F=3 one. Two independent photodetectors are used, one for each detection stage. Four ribbon shaped beams are aligned at this purpose two by two. In their downward trajectory the atoms first see a standing wave laser beam, resonant on the cycling transition $F=4 \rightarrow F'=5$, that is used to detect the atoms in F=4 state; secondly see a progressive wave beam resonant on the same transition that blasts away the detected atoms. In the second detection stage they interact firstly with a pumping beam, that transfers F=3 atoms in F=4 state, and finally with another standing wave beam, resonant on the cycling transition $F=4 \rightarrow F'=5$, that is used to detect the atoms previously in the F=3 state. The relative intensity of the two standing waves is carefully adjusted to get the same detection efficiency. The two TOF signals are used to directly calculate the transition probability after the microwave interaction.

The trapping and the detection chamber is fastened to the lower flange of the external vacuum system; a smaller Conflat transition machined on this flange connects the chamber to the rest of the UHV interaction region. The Ramsey interaction region consists of two identical microwave cavities and a meter tall drift tube; the whole structure is realized in OFHC copper. Thermal conduction with the cryostat is achieved using an aluminum plane that tightly connects the bottom of the cryostat with the body of the cavities. On the cryostat's top another aluminum plane closes the interaction region creating a closed low temperature chamber. Despite this design, few thermal flow channels (such as microwave cables and wiring) affects the insulation. Consequently, the temperature of the interaction region is constantly several degrees above the liquid nitrogen temperature, with a temperature gradient of 1.5 K along the drift tube. The temperature of the interaction region is monitored by three high accuracy Pt-100 sensors placed between the state selection and the Ramsey cavities, at the atoms' apogee and at the top of the drift tube.

Figure 4a shows the temperature of the interaction region over 110 days: nitrogen refills occur three times a day. The larger peaks in figure 4a correspond to the substitution of an empty dewar that caused a liquid nitrogen refill missing. Figure 4b shows the temperature stability of the Ramsey cavity.

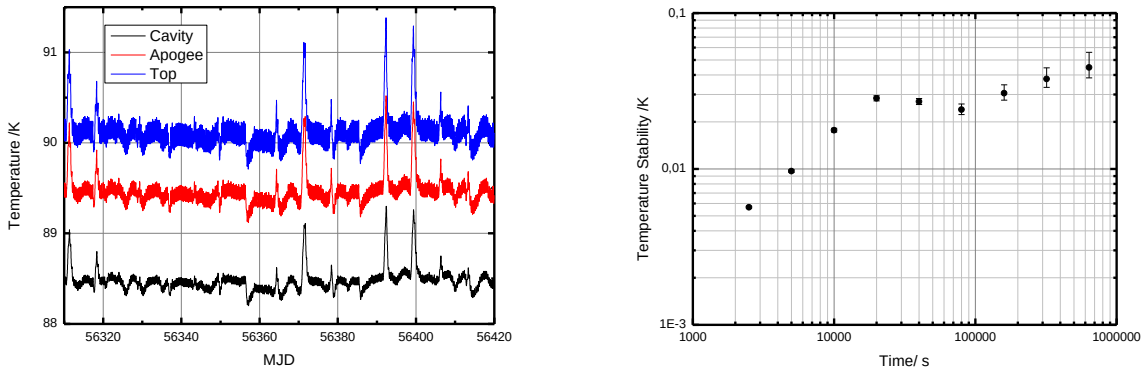

(a) (b)

Figure 4. Temperatures of the interaction region (a) and temperature stability of the Ramsey cavity (b).

The Ramsey cavity design is quite similar to that of ITCsF1 and a detailed description can be found in [21]. It is 60 mm in diameter and 21.8 mm tall. Four feedings are placed on its equatorial plane, each separated by 90° from the other. The feeds are supplied two-by-two through a bent rectangular waveguide cavity matched on the external wall of the Ramsey cavity. The cavity loaded quality factor is Q_L =17000 at room temperature and Q_L =42000 at 88 K, in agreement with the values of Cu losses reported in literature at the two temperatures [19]. Similar values have been measured for the state selection cavity, placed few centimeters below the Ramsey one.

Since the cavity was manufactured and tuned at room temperature to be resonant with the Cs clock transition at 80K, a small error in the copper Thermal Expansion Coefficient led to a detuning of approximately 1 MHz at the operation temperature achieved; also the final temperature eventually achieved by the cavities was 8 K higher than expected. However, this problem does not result in a major limitation of the standard final accuracy.

The vacuum in the interaction region is maintained with an ion pump (20 liter/s) and a Ti sublimation pump, moreover the cryogenic environment helps to maintain the vacuum level, reducing the structure degasing and condensing some residual gases (cryo-pumping). The achieved vacuum level is constantly below the sensitivity of the measurement gauge ($<10^{-7}$ Pa).

Outside the drift tube, a one meter long solenoid generates the magnetic C-field, typically 150 nT in ITCsF2. A long vertical coil placed inside the C-field solenoid, is used to excite a low frequency magnetic field, driving Majorana transitions at 540 Hz. between $|F=3, m_F=0\rangle$ and $|F=3, m_F=\pm1\rangle$ states. These transitions are exploited to map and monitor the magnetic field. The interaction region is shielded by the external magnetic fields through three layers of μ-metal; the two innermost shields are located in the cold region (inside the cryostat), the third is at room temperature (outside

the cryostat). The uniformity and the stability of the magnetic field are discussed later, when the evaluation of the Zeeman shift is described.
The vertical alignment of the fountain is guaranteed by the mechanical construction with respect to a reference plane with 0.05 mrad uncertainty. The reference plane alignment is then set horizontal with a high quality level with 0.125 mrad resolution.

2.2 Laser Setup

The complexity of the accuracy evaluation of a PFS needs a very reliable optical set-up to allow long measurement campaigns.
The optical set up was designed to control all the relevant parameters for optimal atomic manipulation, and to allow long term operations without maintenance and optical realignment. The latter is aided by good temperature stabilization of the laboratory hosting the ITCsF2 .
The optical setup is based on a MOPA system consisting of a 150 mW DFB diode laser and a tapered amplifier: the frequency stabilization is accomplished locking the laser to the Cs saturated absorption crossover dip between $F=4\rightarrow F'=X_{45}$, which is 125 MHz red detuned compared to the cycling transition $F=4\rightarrow F'=5$ used for Cs cooling.
The transition is observed with a modulation transfer technique where the saturating beam is shifted by -80 MHz and Frequency Shift Key (FSK) modulated with an Acusto-Optic Modulator (AOM); in this way, the laser frequency is 165 MHz red detuned compared to the cycling transition. The successive double-pass AOM stages, used to realize the six molasses trapping beams, add +160MHz achieving a total red detuning of few MHz, as needed for optimum Doppler cooling. A PC controlled digital loop permits very long-term reliable operation of the master laser.
The master laser power is split in two beams: the first is used to generate the detection beams, the second to seed the tapered amplifier. The MOPA output is then coupled into a PM fiber to avoid long air path across the optical table and to filter the MOPA mode which is far from being Gaussian. At the fiber output, 220 mW laser light is split to feed 6 double-pass AOM systems [22] corresponding to the 6 laser beams used for the molasses generation. Reshaping the laser beams after the fiber with Galilean telescopes allows for optimal coupling with the AOMs and for 70% efficiency in the double pass. The light is then injected in 6 polarization maintaining (PM) fibers and delivered to the collimators; the overall efficiency of each branch is $\approx 55\%$, so each fiber output power is typically 15mW.

A commercial extended cavity diode laser locked on the Cs F=3→ F'=4 transition is used as repumping laser. A first harmonic saturation spectroscopy, with Doppler profile subtraction, is used for the laser frequency locking.

The optical bench design was conceived for a continuous active control of the 6 laser beams power. In fact, for an accuracy target in the low 10^{-16}, repeatable number of loaded atoms is a fundamental goal for precise density shift measurements. Six independent active servo systems (100 kHz bandwidth) stabilize the laser beams power, also implementing the laser amplitude ramps during the post cooling process. Figure 5 shows the laser amplitude noise spectrum, with and without the servo system activation.

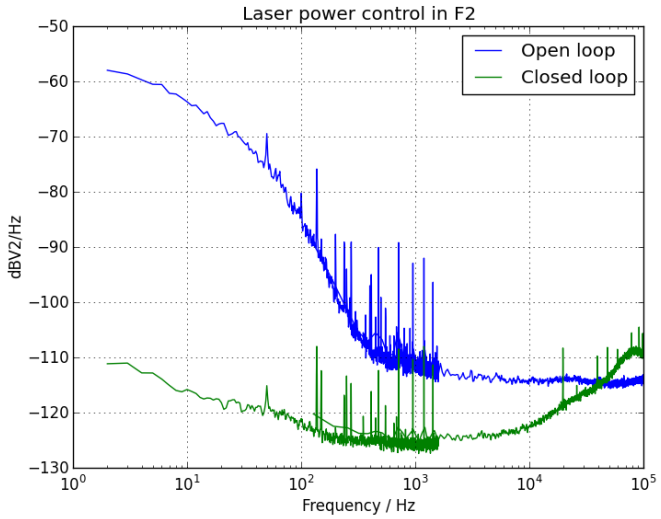

Figure 5. Amplitude noise spectrum of a molasses laser beam, with and without power servo system.

2.3 Operation of the primary frequency standard

ITCsF2 is operated with two distinct software, the first one drives the pattern generator and the DDS parameters of the various AOMs, the second drives the fountain cycle, the TOF signals digitalization, the clock frequency lock loop and all the other clock configuration parameters (i.e. the pattern generator file, the microwave power, the amplitude ramp for the post-cooling, the measurement time, the elapsed time among magnetic field sampling etc.). This architecture allows high flexibility in choosing the proper differential measurement sequences, permitting to concatenate an arbitrary number of different configurations in a recursive cycle.

Considering the hardware, a PC board is used as the main board for I/O signal, whilst a second home built system [23] contains the pattern generator and six DDS modules, used to drive the trapping and the detection AOMs.

As a result, during the accuracy evaluations the frequency of the H-Maser reference has been measured for more than 20 days, with a dead time of few hours only.

The operation cycle of ITCsF2 is similar to that of other fountains. A variable number of atoms is first captured in a (1,1,1) molasses ad then transferred in a vertical moving frame, with a velocity of 4~5 m/s. In this new frame atoms are further cooled with the Sisyphus cooling mechanism to a temperature of the order of 1μK; atoms are then released from the molasses in the free flight trajectory. A microwave state selection is implemented before entering the Ramsey cavity: a microwave π pulse transfers the atoms from $|F=4, m_F=0\rangle$ to $|F=3, m_F=0\rangle$. A subsequent light pulse removes from the cold atom cloud the remaining atoms in the F=4 manifold; all lasers are then switched off by the AOMs and the mechanical shutters, and the Ramsey interaction begins. Atoms pass the Ramsey cavity with a speed of ≈2 m/s and reach the apogee of the ballistic flight approximately 40 cm above the Ramsey cavity; on the way down they pass again in the Ramsey cavity for the second interaction before leaving the cold part of the fountain and entering in the detection chamber where the transition probability is measured.

3. Accuracy Evaluation

In this part of the paper the accuracy budget is discussed, i.e. the measurement of the magnitude and the associated uncertainty of the different physical effects that contribute to the frequency accuracy of the PFS.

3.1 Atomic density shift

As it is well known, collisions between cold atoms produce a relevant shift on the clock transition and, if the time evolution of the atomic cloud is constant, this shift is linearly proportional to the atomic density.

To evaluate this shift we vary the number of launched atoms and accomplish a differential measurement between two different states: high and low density [6]. When operated at high density the short term stability of IT-CsF2 is typically $2\times10^{-13}\tau^{-1/2}$, whilst at low density the stability is typically reduced by a factor 2.

Among several possibilities, we chose to change the number of atoms setting different loading times. The most important advantage of this choice is the shorter clock cycle time in the low density regime, allowing then a better stability. However, to ensure the linearity of the method, it is necessary to verify that the shape and the initial position of the molasses do not change between the

two states. This is done recording the TOF signal on the way up and on the way down for different loading times. The high and low density TOFs are statistically indistinguishable, indicating that the time evolution of the molasses do not change between the two conditions. Figure 6 shows the recorded TOFs.

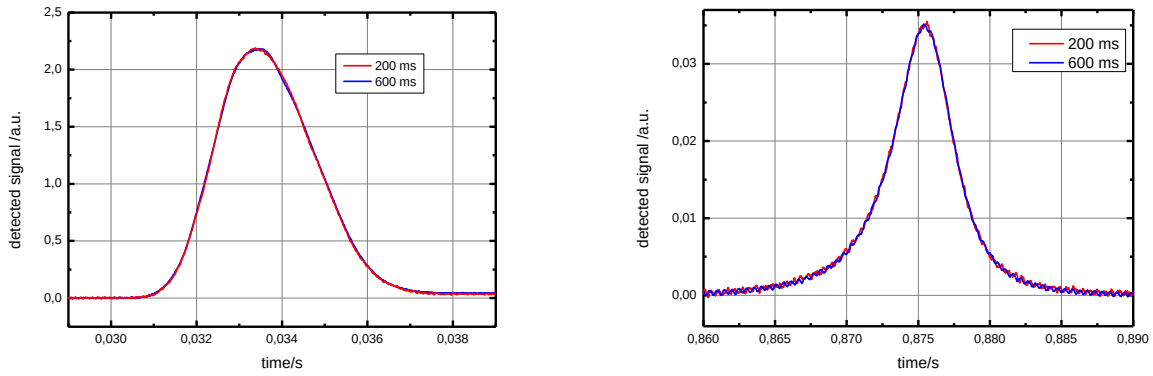

(a) (b)

Figure 6. TOF signals at high and low density on the way up (a) and on the way down (b). Once renormalized the two signals are undistinguishable.

On the contrary, the position of the molasses slightly depends on the loading time; using the high sensitivity of the Ramsey spectroscopy this effect have been precisely measured. Figure 7 shows the displacement of the 30th fringe corresponding to a change in the Ramsey time of 100 μs. Assuming the launching velocity to remain constant, the change in the initial position of the molasses barycenter measures 0.1 mm. The increase of the loading time moves slightly up the barycenter of the molasses; however, this small change produces no significant nonlinearities. Considering for example the value of the Zeeman frequency shift due to the different trajectories of the atoms in the magnetic field profile, the frequency shift among the two situations is less than 10^{-18}.

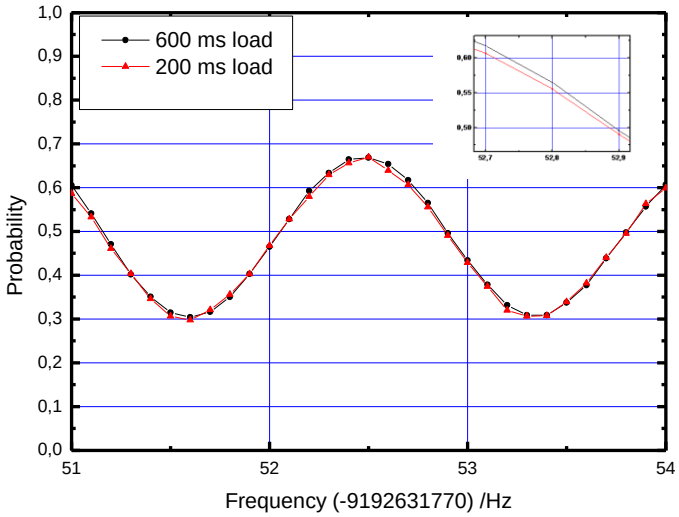

Figure 7. Detail of the 30th fringe frequency recorded with the fountain operated at high and low density. In the inset the frequency displacement is made evident.

Another effect that depends on the number of atoms is the first order cavity pulling [24]. However, also this effect is linear with the atom number and hence the extrapolation to "zero density" is accomplished together with the density shift. The theoretical magnitude of the cavity pulling (as shown later on) is 10^{-17}.

To obtain the best uncertainty, zero density shift extrapolation is evaluated with data collected over a whole TAI evaluation (typically 20 days), together with the historical data collected during previous evaluations. In ITCsF2, we have observed that the detected signal stability is better than 1% for extended periods of time, allowing a good coherence in the historical data set.

When the fountain is at low density, figure 8, the average density shift relative to the Cesium clock frequency ν_{Cs} is typically

$$\frac{\delta\nu_{coll}}{\nu_{Cs}} = (-3.2 \pm 1.3) \times 10^{-16}$$

whilst when the fountain is in the high density regime the shift is three time larger.

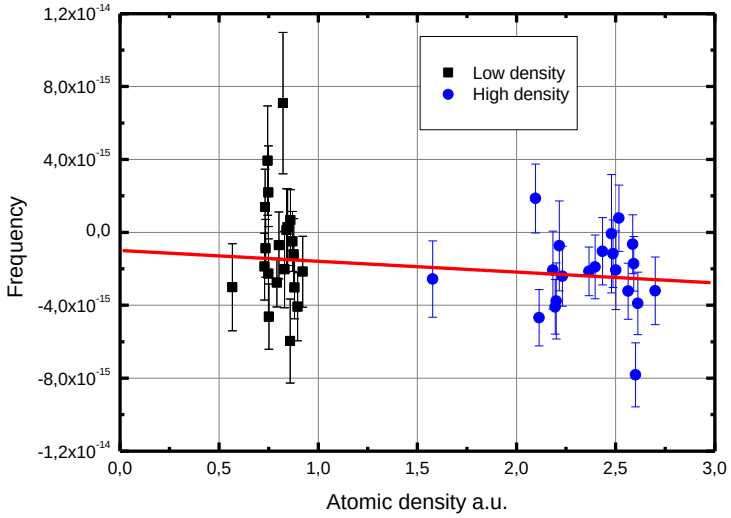

Figure 8. Frequency measurement at high and low density. The Maser drift has been removed.

3.2 Magnetic field

The Zeeman effect induced by the C-field is measured and controlled at the desired uncertainty level by a careful mapping of the C-field and by the constant monitor of its average value.

A shielding test has shown an attenuation of the external magnetic field of about 30000 on the orthogonal direction of the C-field and of 2000 on the parallel axes.

The magnetic field map is obtained exciting the low frequency Majorana transitions $|F=3, m_F=0> \rightarrow |F=3, m_F=\pm 1>$. A short rf pulse (100 ms) is applied when the atoms reach their apogee and the Rabi transition probability is measured. This measurement gives a local value of the magnetic field, since the atoms sample a region of few centimeters at their apogee at a time. Launching the atoms at different heights, it is possible to map the field along most of the interaction region. Once this map is realized, it is used to predict the frequency of the central Ramsey fringe of the magnetic sensitive transition $|F=4, m_F=1> \rightarrow |F=3, m_F=1>$ at arbitrary launching heights.

The discrepancy between the predicted position of the Ramsey pattern central fringe in the $|F=4, m_F=1> \rightarrow |F=3, m_F=1>$ transition, and the measured one is typically ≤ 200 mHz.

Once the central fringe of the magnetic sensitive transition is identified, its value is used to determine the value of the Zeeman shift on the clock transition. Figure 9 shows the typical C-field map for ITCsF2.

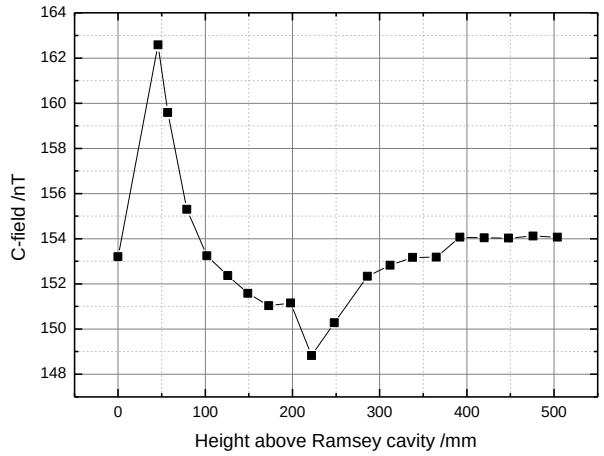

Figure 9. Map of the C-field of ITCsF2 .

Figures 10 and 11 show the short and the long term behavior of the field. It is present a daily fluctuation of the average field at the level of 100 pT; moreover, rarely abrupt field variations occur, as large as 0.2 nT, uncorrelated with the recorded environmental parameters. Thus, it is necessary to monitor every few thousands seconds the value of the magnetic field. However, even if rare, fluctuations are large enough to cause a full fringe jump and, consequently, it is not reliable to use the $|F=4, m_F=1> \leftrightarrow |F=3, m_F=1>$ central fringe frequency to monitor the magnetic field. To track the magnetic field unambiguously, a Majorana transition is continuously excited along the whole flight time of the atoms, and from this measurement the value of the field is inferred. As a matter of fact, it is easier and faster to perform this measurement unambiguously, since only one peak is present and a full map is not needed to identify the central fringe. This automated measurement is typically performed every 2500 s.

The Majorana resonance transition is not a good representation of the magnetic field along the Ramsey flight, because the amplitude of the applied field can change from place to place and its penetration depth in the interaction region is not constant (because of different wall thickness).
Consequently, a wrong weight of the local field along the atom free flight is expected. Nonetheless, for small fluctuations of the magnetic field, an excellent linearity was observed between the magnetic field value measured with the Ramsey spectroscopy and the Majorana measurement; once calibrated, this allows to precisely track the field variations. The calibration between the Majorana measurement and the Ramsey central fringe value in the magnetic sensitive transition is periodically repeated with a full map process taking few hours of measurement.
Figure 10 shows the value of the central frequency of the Majorana transition, whilst figure 11

reports its frequency stability. As already said, the C-field is monitored with a period of 2500 s: at this measurement time, the stability of the magnetic field is around 0.05 nT; considering a C-field value of 1.5 $\times 10^{-7}$ T, this results in an uncertainty on the clock transition frequency of 0.7×10^{-16}.

Since the magnetic sensitive transition is used to determine the Zeeman shift, an additional contribution to the bias uncertainty is the difference Δ_B between the time average of the squared magnetic field B and the square of the time averaged field:

$$\Delta_B = \frac{1}{T}\int_0^T B^2\, dt - \left(\frac{1}{T}\int_0^T B\, dt\right)^2 \quad (1)$$

where T is the Ramsey time, as the time averaging is on the ballistic flight of the atoms.

From the analysis of the recorded C-field map, shown in figure 9, the difference is $\Delta_B \leq 6.5\times10^{-18}$ T^2; using the sensitivity coefficient of the second order Zeeman shift (427.45×10^8 Hz/T^2), the contribution to the bias uncertainty is $\leq 3\text{x}10^{-17}$.

Combining all the contributions, the total uncertainty for the magnetic field correction is 0.8×10^{-16}.

Therefore, the second order Zeeman bias $\delta\nu_Z$ relative to the Cesium clock frequency ν_{Cs} is

$$\frac{\delta\nu_Z}{\nu_{Cs}} = (1075.0 \pm 0.8)\times10^{-16}$$

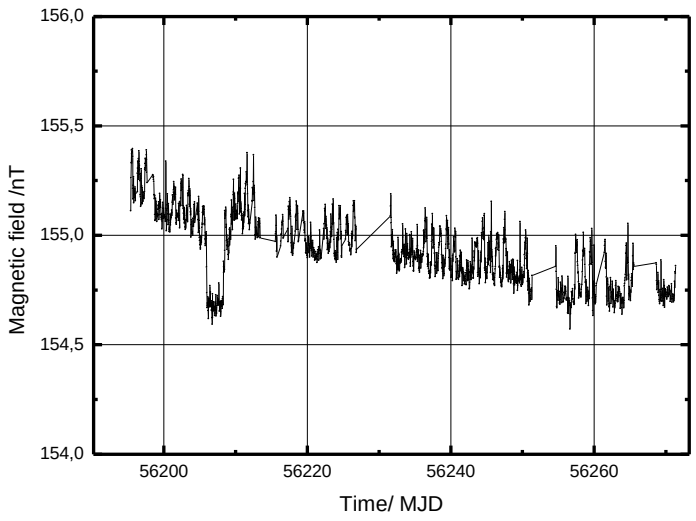

Figure 10. C-field amplitude measured with Majorana transition, recorded over three months of ITCsF2 operation. The fast oscillations are observed on a daily period. Abrupt field changes like the one observed at MJD 56206 are well controlled with the Majorana spectroscopy.

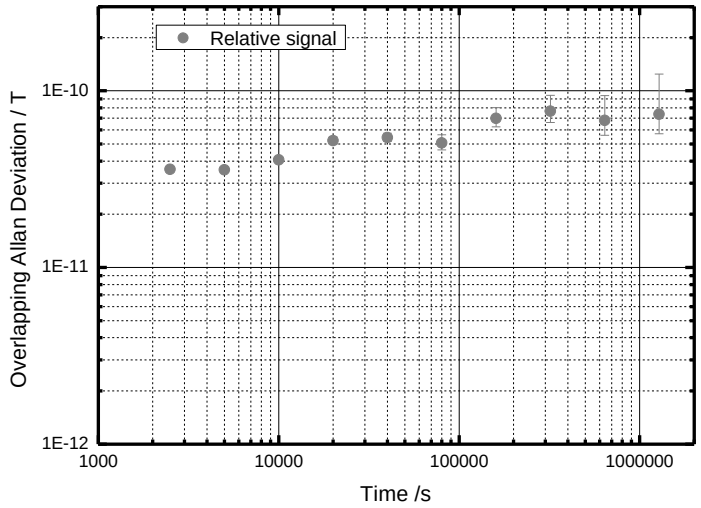

Figure 11. Long term stability of the time averaged magnetic field.

3.3 Blackbody radiation

The blackbody radiation shift is strongly reduced in ITCsF2 compared to other PFS, because of the cryogenic temperature of the interaction region. As discussed in the physical package description, the temperature is measured with three Pt100 sensors, one placed between the state selection and the Ramsey cavities, a second 50 cm above, nearby to the atom apogee, and a third at the top of the drift tube.

The interaction region of ITCsF2 is to, a good approximation, a blackbody radiator. In fact, there is only a single aperture to the external environment at room temperature, that is the lower hole of the state selection cavity, 10 mm in diameter. Moreover the structure design is conceived to strongly reduce the radiation propagation at low reflection angles within the drift tube. This implies that cesium atoms interact with the room temperature radiation at a very small solid angle. For an atom in the Ramsey cavity, the bottom aperture to the external environment is a diaphragm of 1 cm diameter at a distance of 10 cm, corresponding to a solid angle of 6×10^{-4} sr. Rising the drift tube, this solid angle decreases further till $4x10^{-5}$ sr at apogee [25].

The average temperature in the drift tube is 89.4 K, stable within 100 mK. The thermal gradient along the tube is <2 K, which is also considered as the temperature uncertainty.

The Blackbody radiation shift $\delta\nu_{BBR}$ relative to the clock transition frequency ν_{Cs} is evaluated using the well-known relation

$$\frac{\delta\nu_{BBR}}{\nu_{Cs}} = \beta\left(\frac{\Theta}{300}\right)^4\left[1+\varepsilon\left(\frac{\Theta}{300}\right)^2\right] \qquad (2)$$

where Θ is the blackbody temperature, β=-1.711(3) 10^{-14} and ε=1.3(1) 10^{-2}[26-27]. As the thermodynamic temperature of ITCsF2 drift region is Θ=(89.4 ± 2) K, the blackbody radiation shift is $(-1.36 \pm 0.09)\times 10^{-16}$. Taking into account the small solid angle aperture to the external environment at room temperature (296 K), the final correction is:

$$\frac{\delta\nu_{BBR}}{\nu_{Cs}} = (-1.45 \pm 0.12)\times 10^{-16}.$$

3.4 Gravity

INRIM's laboratories elevation was accurately measured in 2007 during a leveling campaign reported in [28].

The atom apogee in ITCsF2 has an orthometric elevation h= (238.71 ± 0.10) m on the Geoid. As INRIM site is located at 45° 00' 54.467'' N latitude and 7° 38' 21.842'' E longitude, the relative frequency sensitivity to the orthometric height is 1.0911×10^{-16} m^{-1}, evaluated from the local absolute gravity acceleration on the Geoid, g = 9.806 32(1) ms^{-2}. The frequency shift $\delta\nu_G$ relative to the cesium clock frequency ν_{Cs} for ITCsF2 integrated along the free flight trajectory, is:

$$\frac{\delta\nu_G}{\nu_{Cs}} = (260.4 \pm 0.1)\times 10^{-16}$$

3.5 Microwave generation and related shifts

The design of the microwave synthesis and distribution and the assessment of its spectral performances are a relevant issue for a microwave PFS. In fact, the microwave related shifts are the main contribution to ITCsF2 accuracy.

In a proper design, spurious components of the microwave spectrum must be negligible; also, microwave leakages from the synthesizer during the atom free flight must be avoided; any modulation of the microwave frequency must not produce any thermal transient resulting in a microwave phase variation between the first and the second Ramsey pulses; the Dick effect must be

minimized.

The microwave synthesis chain was designed taking into account the previous requirements. Its scheme is shown in figure 12. Starting from the 5 MHz generated by a BVA quartz phase locked to a H-Maser, a direct synthesis scheme produces the intermediate 100 MHz frequency using two multiplications modules (x4 and x5). A Dielectric Resonant Oscillator (DRO) provides the 9.2 GHz carrier, then phase locked to the 100 MHz signal. Thereafter, to obtain the 9.192 Cs frequency, a single sideband mixer (SSB) subtracts from the carrier the 7.4 MHz signal generated by a Direct Digital Synthesizer (DDS). Two identical synthesizers were developed, one for the Ramsey excitation and one to feed the state selection cavity.

The measured spectrum is shown in figure 13. Undesired shifts from spurious components are excluded, since the only detected components are at 50 Hz and its harmonics, whose power is highly symmetric with respect to the carrier. The presence of spurs very close to the carrier, possibly coming also from the fountain cycle, can be observed detecting the spectrum of the beat note between the two independent synthesis chains. No spurious lines were detected except the 50 Hz harmonics.

Figure 14 shows the stability of the synthesis chain in terms of the overlapping Allan deviation. In the medium term, the stability is limited by the temperature phase sensitivity of the first multiplication stage.

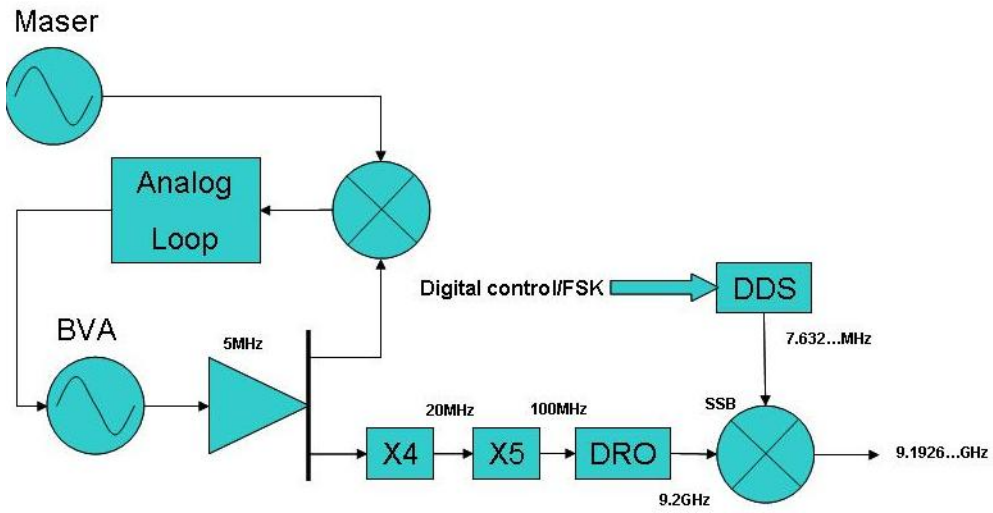

Figure 12. Scheme of the synthesis chain used in ITCsF2.

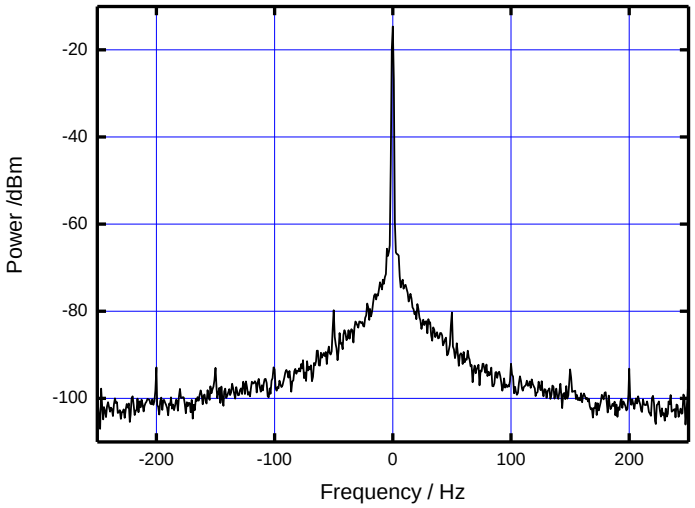

Figure 13. RF Spectrum of the synthesized microwave

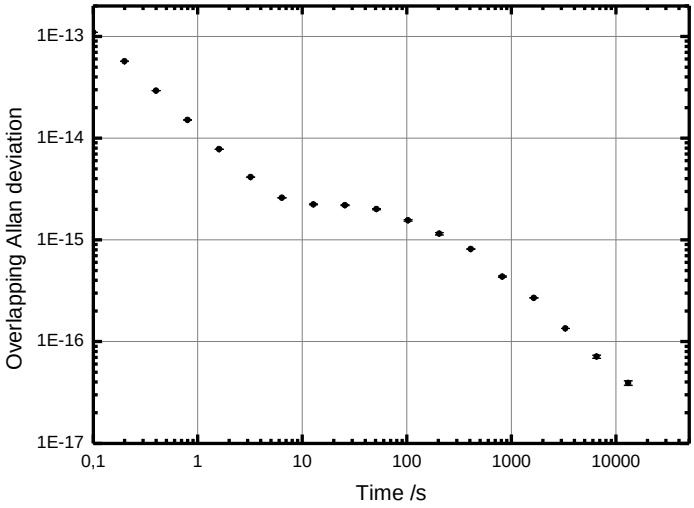

Figure 14. Frequency stability of the synthesizer.

To ensure that the resonant microwave radiation interacts with the atoms only in the microwave cavities, once the atoms are outside a cavity, the microwave is detuned using FSK modulation. FSK modulation is applied on the DDS frequency at the rf input of the SSB mixer at constant amplitude. No power change is induced in the mixer, avoiding the phase rotation due to the temperature transients. The modulation is applied to the state selection synthesizer immediately after the Rabi pulse. The FSK modulation is applied to the main synthesizer when the atoms exit the Ramsey cavity on their way down.

Following the work reported in [17] ITCsF2 has been tested at varying microwave power and in

different experimental condition.

In a first test, a given microwave pulse was applied to the atoms only once, while they were rising or while they were descending. A difference in the transition probability was observed and it is shown in figure 15 for different values of the microwave pulse. Whereas Rabi oscillations are evident, a slight difference in the transition probability is observed at any given excitation amplitude between the upward and downward cavity passage. Higher the microwave power, larger the difference. To allow a straight comparison of the experimental results with the developed theory, the power was then kept constant at 5/2 π Ramsey pulse.

Therefore to avoid any ambiguity, to set a given pulse amplitude we decided to scale it proportionally to π/2 pulse amplitude and not to measure the transition probability.

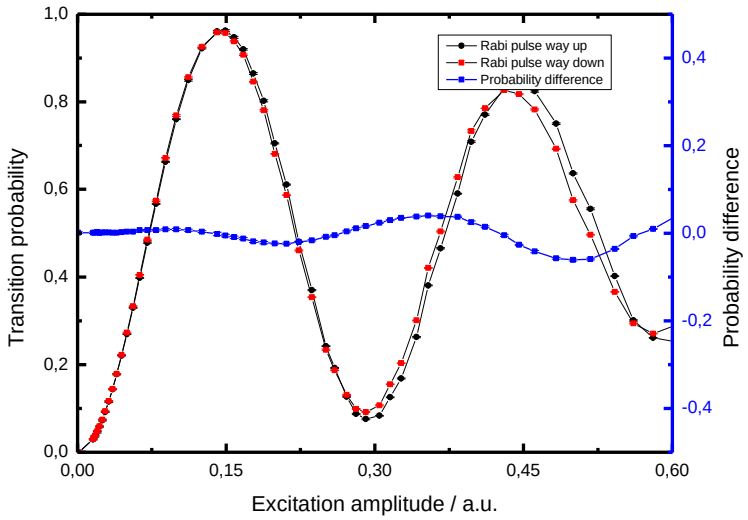

Figure 15. Transition probability with an exciting pulse of variable amplitude applied either on the way up or down (left vertical scale). The blue line (right vertical scale) represents the excitation probability difference.

3.6 Microwave leakage

Two different kinds of microwave leakages may be present in a fountain frequency standard.

The first kind is typically created by dispersed fields present in the drift tube and then occurs between the two Ramsey interactions, almost symmetric because of the trajectory path reversal . The second one happens when a microwave field is present before or after the Ramsey interaction, and it is hence intrinsically asymmetric. ITCsF2, implements several design solutions to reduce the overall leakage. The Ramsey cavity is joined to the drift tube by a cylindrical waveguide, 5 cm long

and 1 cm in diameter, that provides a nominal attenuation of 150 dB [15]. On the top of the drift tube a similar system with a slightly larger diameter has an attenuation of 30 dB. The latter is probably a limitation and a replacement is planned to get a higher attenuation.

The leakage can be observed measuring the frequency shift of the clock transition at pulses ≠ (2n+1) π/2. As described in [15], this type of leakage has a linear frequency sensitivity around the optimal excitation amplitude, shown in figure 16(a). Table I reports the measured sensitivity at high pulses, proportional to the pulse amplitude within the stated uncertainty.

Pulse amplitude	DDS Amplitude (mV)	Sensitivity 10^{-15}/mV
π/2	39.9	0.085±0.081
3/2 π	119.7	0.37 ±0.07
5/2 π	199.5	0.55 ±0.06

Table 1. Power sensitivity around optimal excitation pulses.

Note that it is incorrect to compare the data at various pulses amplitude of figure 16(a). In fact, differential measurements were separately performed at π/2, 3π/2 and 5π/2, alternating one pulse amplitude to another. Between different dataset there is a temporal separation ranging from few days to few weeks. In these periods, the maser drift is accumulated and only roughly corrected. For this reason a separate differential measurement was tested at (2n-1)π/2, as reported in figure 16(b).

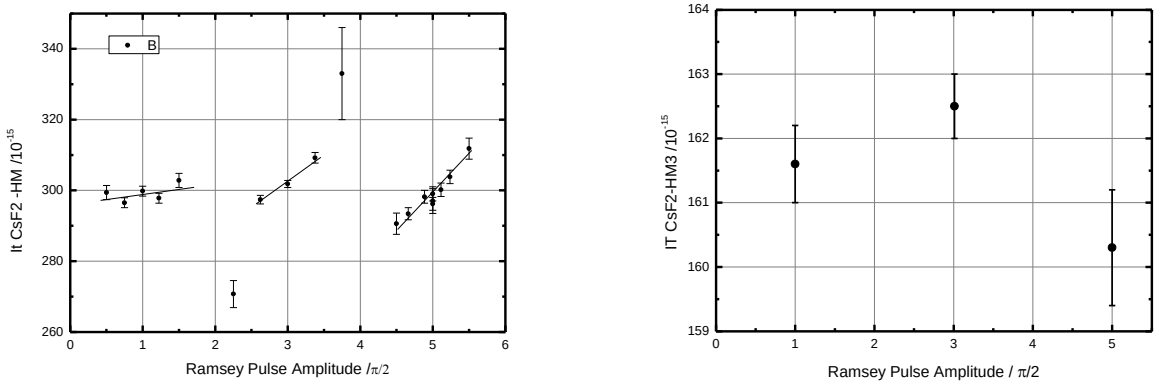

(a) (b)

Figure 16. Relative frequency sensitivity to excitation field. (a) pulse amplitude varied around the nominal value, (b) pulse amplitude set to maximize the transition probability.

To confirm that the shift measured is consistent with leakage during the Ramsey time, the measurement was repeated inserting in the microwave feeding line an interferometric switch [16], that can attenuate the microwave output between the two Ramsey interactions by 50 dB, without

significant effects on the microwave phase at the 10^{-15} level. As expected a strong reduction of the sensitivity was observed. Nevertheless the switch is not used during normal fountain operation because it is not yet fully characterized at the microradiant level.

The measurement was repeated at the nominal excitation powers and interpolated with the function $\delta\nu/\nu \propto n \sin(n\pi/2)$. The behavior described by the previous function is valid not only for the microwave leakage, but also for other effects like the lensing effect and, partially, the distributed cavity phase shift. According to the experimental data reported in figure 16(b), the frequency shift $\delta\nu_{leak}$ relative to the Cesium clock frequency ν_{Cs} for ITCsF2 is:

$$\frac{\delta\nu_{leak}}{\nu_{Cs}} = (-2.0\pm1.5)\times10^{-16}$$

3.7 Distributed cavity phase shift (DCP)

Another effect that may limit the accuracy of fountains PFS is the distributed cavity phase (DCP) shift.

DCP shift is caused by the microwave power flowing in the cavity. Specifically, due to losses in the cavity conducting walls, a small travelling wave is superimposed to the standing wave defining the electromagnetic mode. This travelling wave is responsible of a spatially varying phase shift, so that different atomic trajectories interact with a different phase, resulting in a shift that affects the clock frequency.

From a mathematical point of view, the magnetic component $\mathbf{H}(\mathbf{r})$ of the electromagnetic mode can be written as:

$$\mathbf{H}(\mathbf{r}) = \mathbf{H}_0(\mathbf{r})+(\Delta\omega_C/\Gamma+i)\,\mathbf{g}(\mathbf{r})/(1+\Delta\omega_C^2/\Gamma^2) \quad (3)$$

where $\mathbf{H}_0(\mathbf{r})$ represents the standing wave satisfying the boundary conditions of a perfect conductor for a well specified mode (TE_{011} in ITCsF2), $\mathbf{g}(\mathbf{r})$ is a small dissipative field, Γ is the half-width of the cavity profile at half maximum and $\Delta\omega_C$ is the cavity detuning from the clock frequency. A similar expression holds for the electric field component.

The source of the DCP shift is $\mathbf{g}(\mathbf{r})$ that is weighted by the cavity profile, as shown in Eq. (3). As already mentioned in the physical package description $\Delta\omega_C$ is $\approx 4\Gamma$ for ITCsF2. Consequently, the imaginary component of the field responsible of the DCP shift is reduced compared to the situation of the on-resonance cavity (see Eq. (3)). However, we notice that in the off-resonance case more

power is required to flow into the cavity to excite the mode of interest to a given level (namely to produce $\pi/2$ pulses). Also, the degenerate mode TM_{111} may play a significant role in the evaluation of the DCP shift in the off-resonance cavity, even despite the presence of mode chokes.

However, we can state that, in general, the high quality factor (45000 for ITCsF2) compensates to a good extent the drawbacks of the higher driving power compared to what is reported in other Cs fountains. [4-7-8-17].

To gain physical insight into the evaluation of DCP shift, we consider the approach reported in [18] in which $\mathbf{g}(\mathbf{r})$ is expressed in terms of an azimuthal Fourier modal expansion:

$$\mathbf{g}(\mathbf{r}) = \Sigma_m g_m(\rho, z) \cos(m \phi) \quad (4)$$

The modal expansion (4) converges rapidly and it is sufficient to analyze the first three terms m=0, 1, 2.

The m=0 mode is not generally expected to give a significant DCP shift when the cavity is fed symmetrically; ITCsF2 cavity has four feeds evenly spaced on the equatorial plane and, moreover, the high quality factor reduces the power flow to the walls.

The effect of the m =1 mode produces a DCP shift since the average trajectories of the atoms and the phases of the field on the two passages are different. According to the analysis reported in [30-31], the effect of this modal component has been tested by enhancing the asymmetry of the feeding system and by measuring its effect on the clock transition for different vertical tilting of the fountain with respect to the perpendicular.

ITCsF2 cavity is fed by four iris placed at 90° and coupled two by two with two distinct external waveguide cavities. This feeding method guarantees a quite good phase and amplitude balance on each couple of feeds. As reported in [30], a high sensitivity measurement consists in the analysis of the difference between “North” and “South” feeding at increasing power and different tilting, where the “North” direction is identified by one couple of feeds and the “South” direction by the other couple. We performed this measurement tilting the fountain on the North-South axis and on the East-West axis. Figure 17 shows that the tilting sensitivity at the optimum power ($\pi/2$) on North-South axis is $(0.2 \pm 0.2)\times10^{-15}$/mrad, whilst on the East-West axis the sensitivity measures $(1.2\pm0.5)\times10^{-15}$/mrad.

The fountain is on the perpendicular on both axes within 0.125 mrad by construction, but the measured tilt sensitivity allows to state that the system is vertically aligned at the level of 50 μrad. The power balance between left and right feeding is better than 1% and the maximum shift due to the combined effect of vertical misalignment and m=1 mode of the DCP field expansion is

$\leq 1\times10^{-17}$.

Another test was done at 3π /2 with symmetric feeding, and fountain tilting on the north-south axes. It did not produced a measurable shift at the level of $\delta\nu_{DCP}/\nu_{Cs} = (0.03 \pm 1.2)\times10^{-15}/\,\mathrm{mrad}$. Also this value confirms that the maximum expected shift coming from the *m*=1 term of the mode expansion is below 1×10^{-17} when the fountain is operated at π/2.

According to the theory developed in [30], these measurements provide as well an independent evaluation of the relative phase difference φ between left and right feeding lines:

$$\frac{\Delta\nu_C}{\Gamma}\tan(\varphi) = \frac{Sym(2\varphi) - \frac{1}{2}(Asym1 + Asym2)}{Asym1 - Asym2} \quad (5)$$

where *Asym1* (*Asym2*) is the frequency shift when feeding only from one side (from the other side) and *Sym* represents the clock frequency measurement when feeding with the two lines together (*Sym*= (*Asym1*+*Asym2*)/2). The measurements from the DCP shift characterization give $\varphi = (0.026 \pm 0.023)\,\mathrm{rad}$. This result agrees with an independent measurement of φ, obtained observing the frequency of the Ramsey central fringe when an asymmetric pulse is applied on the North feeding on the way up and on the South feeding on the way down (and vice-versa).

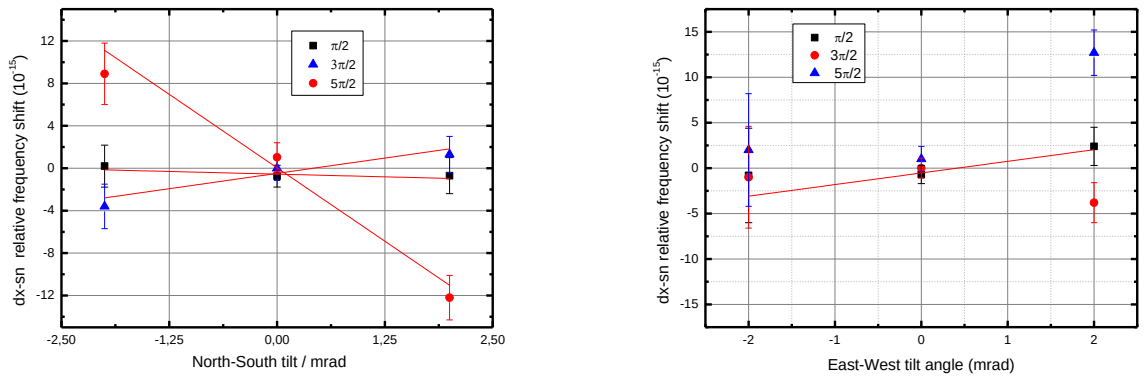

(a) (b)

Figure 17. Frequency sensitivity to vertical tilting of the fountain (a) tilt orthogonal to the feedings (b) parallel to the feedings.

The contribution to DCP of the *m*=2 mode is expected to be highly suppressed by the ITCsF2 feeding geometry (four feeds). This is probably the larger difference between a cavity with two and four feedings with respect to DCP shift.

In conclusion, the total shift $\delta\nu_{MW}/\nu_{Cs}$ associated with microwave imperfections, leakages and

DCP is:

$$\frac{\delta\nu_{MW}}{\nu_{Cs}} = \left(-2.0 \pm 1.5\right)\times 10^{-16}$$

3.8 Cavity Pulling

Since ITCsF2 Ramsey cavity is operated off-resonance, the cavity pulling effect is reduced. Considering the second order cavity pulling, the bias $\delta\nu_{CP2}$ relative to the Cesium frequency ν_{Cs} is described by the formula [32]:

$$\frac{\delta\nu_{CP2}}{\nu_{Cs}} = f(\Delta\nu_C)\frac{1}{\nu_{Cs}}\frac{8}{\pi^2}\left(\frac{Q_L}{Q_A}\right)^2 b\tau\cot(b\tau) \quad (6)$$

where $\Delta\nu_C$ is the cavity detuning, Q_L the cavity loaded quality factor, Q_A the atomic transition quality factor, b the Rabi frequency, τ the Rabi time, and $f(\Delta\nu_C)$ is a function describing the dependence of the shift on the cavity detuning. Even not considering the analytical expression of $f(\Delta\nu_C)$, it is well known [30] that $f(\Delta\nu_C)$ has a dispersive shape and exhibits extreme values for $\Delta\nu_C = \pm\ \Gamma$, being Γ the half-width of the cavity. Thus, a conservative evaluation of the cavity pulling is obtained using the linearization of $f(\Delta\nu_C)$ at the maximum value for $\Delta\nu_C = \pm\ \Gamma$, that is $|f(\Delta\nu_C)| = \Gamma$.
In ITCsF2, the optimal excitation power is set within 1% uncertainty, therefore using Eq. (6) the second order cavity pulling is $<3\times10^{-17}$.
On the other hand, the first order pulling effect, due to the stimulated emission of the atoms inside the cavity, is linear with the atom density. Hence, it is evaluated together with the atomic density shift. An estimate of its magnitude however gives a quite low absolute value. According to the calculations made in [33], the first order cavity pulling $\delta\nu_{CP1}$ can be written as:

$$\frac{\delta\nu_{CP1}}{\nu_{Cs}} \approx -\frac{2}{h}\mu_0\mu_B^2\eta' n\tau\frac{Q_L}{Q_A}\cos(b\tau)\frac{\Psi}{1+\Psi^2} \quad (7)$$

where h is the Planck constant, μ_0 the vacuum permeability, μ_B the Bohr magneton, η' the cavity filling factor, n the atomic density, τ the Rabi time and Ψ is the normalized cavity detuning $\Psi = 2Q_L\Delta\nu_C/\nu_{Cs}$.

In ITCsF2, the filling factor, deduced from [34] is ~0.1, the density is of the order of 10^5 atoms/cm^3, and Ψ is 8; thus, $\delta\nu_{CP1}/\nu_{Cs} < 2\times10^{-17}$.

3.9 Total accuracy budget of ITCsF2

Table 2 summarizes the biases and the uncertainty contributions of ITCsF2. The total type B uncertainty is 1.8×10^{-16} and the type A uncertainty associated with the bias evaluation is 1.3×10^{-16}. The combined uncertainty, i.e. the ITCsF2 accuracy, is 2.2×10^{-16}.

Physical effect	Bias (10^{-16})	Uncert. (10^{-16})
Zeeman effect	1075.0	0.8
Blackbody radiation	-1.45	0.12
Gravitational redshift	260.4	0.1
Microwave leakage	-2	1.5
DCP	-	0.2
2nd order cavity pulling	-	0.3
Total Type B**		**1.8**
Atomic density (typical LD)*	-3.2	1.3
Total	**1328.75**	**2.2**

Table 2. Accuracy budget of ITCsF2 . *The density bias changes from run to run depending on the type of differential measurement performed and on the length of the measurement. ** All other effects not reported here are estimated to have a magnitude $<10^{-17}$.

4. Comparison with TAI

Along with its accuracy evaluation, several frequency comparisons of ITCsF2 to TAI have been performed. The comparison technique is the standard two way satellite link [35] where a local H-Maser (HM) participating to the realization of UTC(IT) is measured by ITCsF2. These frequency data are communicated to BIPM and used to estimate the frequency value of TAI measured by our fountain.

Figure 18 shows the daily data relative to two successive measurements. The PFS is alternatively operated at high and low atomic density on a fixed schedule basis, and then the frequency is extrapolated to zero density. It can be observed that the drift of the maser is quite stable for extended periods of time; its value is 6×10^{-16}/day.

Figure 19 reports the statistical instability of the measurement. The typical Allan deviation is $\sigma_y(\tau) = 2.5\times10^{-13}\tau^{-1/2}$.

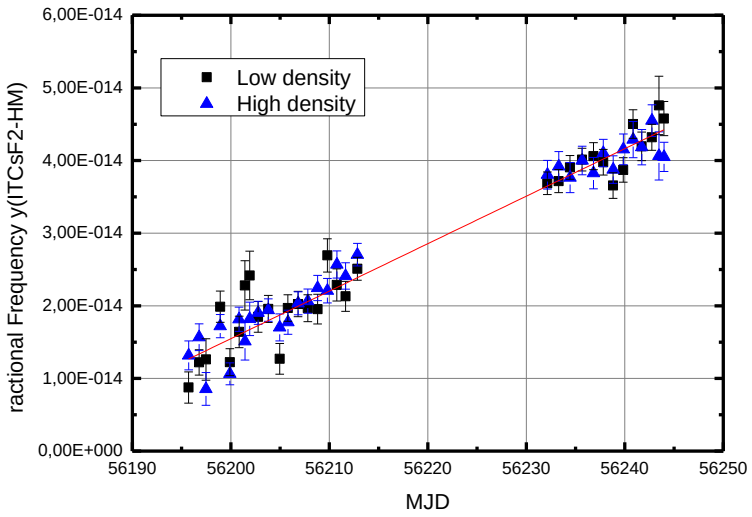

Figure 18. Frequency measurement of ITCsF2 fountain vs. H-Maser.

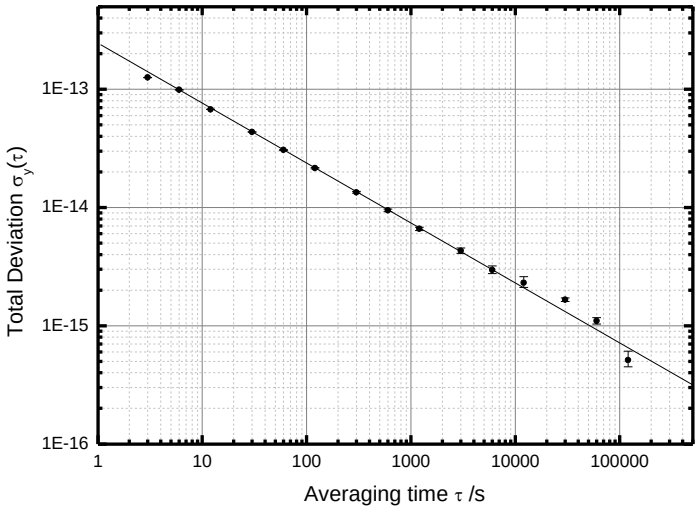

Figure 19. Stability of the fountain when operated at high atomic density regime.

During the reported evaluation period, the H-maser (BIPM code 1401103) was used as local oscillator. After correcting the row data for the biases reported in table 2, the average frequency *<y(ITCsF2-HM3)>* over the measurement period was calculated with a weighted linear fit, with the epoch coordinate origin on the centre of the evaluation interval.

Unavoidable fountain dead (lost) time is present during the evaluation and, in principle, the dead

time may be neither evenly spaced nor symmetric with respect to the centre of the evaluation period. In these conditions, simply averaging the data would produce a bias of the frequency estimation, thus the fitting is needed.

A certain amount of dead time is scheduled to monitor the C-field monitor or to implement additional characterizations during the measurement. The scheduled dead time amounts to 1.5% and it is almost homogeneously distributed.

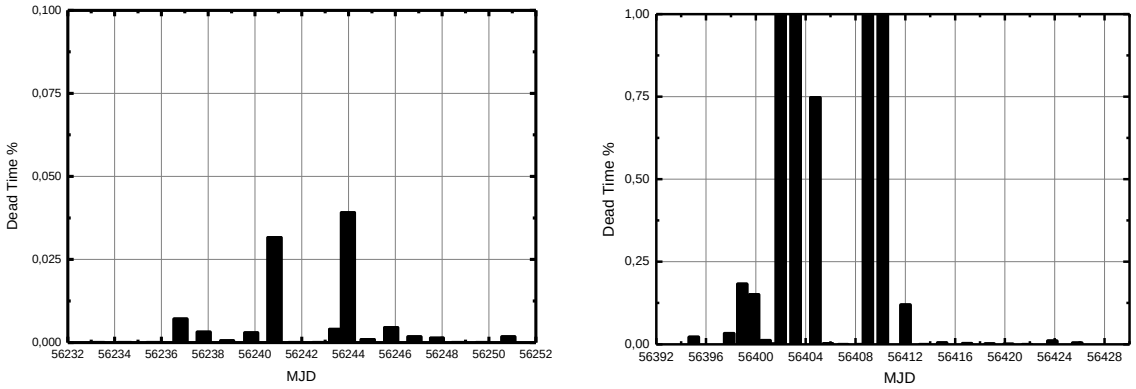

Figure 20. Epoch distribution of unscheduled dead time during two distinct evaluations (note the different vertical scale).

The choice of a linear model for the maser drift is supported by the experimental observation of its stability for extended periods of time (typically several months). The uncertainty associated to the average frequency estimation <*y(ITCsF2-HM)*> is estimated by the least square algorithm.

The dead time in fountain operation (figure 20) introduces a further uncertainty to the frequency comparison. The estimation of this uncertainty contribution requires the knowledge of the H-Maser noise properties. The stability of the H-Maser could be modelled in terms of Allan variance, as:

$$\sigma_y^2(\tau) = \sigma_{yWF}^2(\tau) + \sigma_{yFF}^2(\tau) + \sigma_{yRW}^2(\tau)$$

where $\sigma^2_{yWF}(\tau)$, $\sigma^2_{yFF}(\tau)$ and $\sigma^2_{yRWF}(\tau)$ are respectively the contribution due to the white, the flicker and the random walk frequency noise. A conservative estimation of these contributions is:

$$\sigma_{yWF}(\tau) < 2 \cdot 10^{-13} \tau^{-1/2}$$

$$\sigma_{yFF}(\tau) < 3 \cdot 10^{-16}$$

$$\sigma_{yRW}(\tau) < 2 \cdot 10^{-19} \tau^{1/2}$$

The dead time uncertainty is evaluated implementing the algorithm reported in [36-38]

TAI is a convenient mean to compare ITCsF2 to other PFS worldwide. Therefore, ITCsF2 data were reported to the BIPM to evaluate the frequency difference between the TAI interval unit and ITCsF2. At the same time, BIPM used all the available data provided by PFSs to estimate the value of TAI. Since ITCsF2 is not yet contributing to TAI, this process evaluates the difference between ITCsF2 and the other PFSs without correlations.

The best estimate of the TAI value is monthly reported in the circular T [39]. The results of the comparisons are reported in table 3, where u_A, u_B and u_{lab} are the Type A, the Type B and the dead time uncertainties respectively; *utot* is the combined uncertainty, *d(ITCsF2-TAI)* and *d(circT)* is respectively the frequency difference evaluated by BIPM and deduced from Circular T; Δd is the difference between the two methods. The values are expressed in fractional 10^{-15} units.

Measurement period	u_A	u_B	u_{lab}	u_{tot}	*d* (ITCsF2-TAI)	*d* (circT)	Δd
56079-56099	0.32	0.32	0.2	0.53	2.38	2.5±0.2	-0.12±0.57
56194-56214	0.42	0.21	0.2	0.58	-0.11	-0.2±0.3	0.09±0.65
56234-56249	0.31	0.18	0.1	0.52	-0.93	-0.3±0.3	-0.63±0.60
56394-56424	0.34	0.18	0.2	0.48	-0.2	-0.3±0.2	0.10±0.52

Table 3. Measurements of TAI performed with ITCsF2; the values are expressed in fractional 10^{-15} units

The four measurements reported in table 3 show a good agreement between ITCsF2 and all the other fountains participating to TAI used to steer its frequency. Without knowing the exact weight of the various standards in each TAI computation, it is not possible to discriminate between type A and type B uncertainty and perform an exact statistical analysis on Δd. Nonetheless, the biases of the fountains contributions to TAI are highly uncorrelated, thus *d(circT)* has a pure statistical meaning and could be combined with the statistical component of the fountain, considering fully correlated only the type B uncertainty of ITCsF2. The weighted average $\Delta d = (-0.17 \pm 0.32) \times 10^{-15}$ is obtained. showing a good agreement between ITCsF2 and the other PFS. During the measurement periods reported above, BIPM used data coming from NPL-CSF2, SYRTE-FO1,SYRTE-FO2, PTB-CSF1, PTB-CSF2 and NIST-F1.

Conclusions

We have reported the accuracy analysis of ITCsF2, the new Italian PFS developed at INRIM. ITCsF2 with its twin NIST F2 are the first Cs primary frequency standards operating at cryogenic temperature to reduce the Blackbody radiation shift magnitude and uncertainty. The overall Type B total uncertainty is 1.8×10^{-16}, and the major contribution is coming from imperfections in the microwave excitation scheme. Type A uncertainty is related to the density shift evaluation and to the method used to estimate the average frequency of the flywheel maser. Its magnitude can change from one measurement to another and is typically 3×10^{-16}. The calibrations of TAI performed with our fountain compared to those obtained by the fountains of other National Metrological Institutes are in agreement at the level of 3×10^{-16}.

The primary frequency standard here described is among the more accurate Cs primary frequency standards worldwide developed.

Acknowledgments

We wish to acknowledge S. R. Jefferts, T. P. Haevner and E. A. Donley for their invaluable contribution to the realization of ITCsF2; T. E. Parker for providing comparison data between ITCsF2 and NIST standards; E. K. Bertacco and L. Lorini for their help at different stages of the project; V. Pettiti for providing the Maser data and G. Petit for providing the comparison data against TAI.

References

[1] Clairon A., Laurent P., Santarelli G., Ghezali S., Lea S. N. and Bahoura M., (1995) *IEEE Trans. Instrum. Meas.* **44**, 128-131.

[2] Jefferts S. R., et al. 2002 *Metrologia* **39** 321

[3] Heavner T. P., Jefferts S. R., Donley E. A., Shirley J. H. and Parker T. E., (2005) *Metrologia* **42** 411

[4] Gerginov V., Nemitz N., Weyers S., Schröder R., Griebsch D. and Wynands R., (2010) *Metrologia* **47** 65

[5] Weyers S., Hubner U., Schroeder R., Tamm C. and Bauch A., (2001) *Metrologia* **38** 497

[6] Levi F., Calonico D., Lorini L. and Godone A., (2006) *Metrologia* **43** 545.

[7] Guena J. et al., (2012) *IEEE Trans. Utrason. Ferroelect. Freq. Control* **59** 391.

[8] Li R. X., Gibble K. and Szymaniec K., (2011) *Metrologia* **48** 283.

[9] Kumagai M., Ito H., Kajita M. and Hosokawa M., (2008) *Metrologia* **45** 139 .

[10] Kurosu T., Fukuyama Y., Koga Y. and Abe K., (2004) *IEEE Trans. Instrum. Meas.* **53** 466 .

[11] Wynands R. and Weyers S., (2005) *Metrologia* **38** 34

[12] Parker T. E., (2010) *Metrologia* **47** 1

[13] Jefferts S. R., Shirley J. H., Ashby N., Burt E. A. and Dick G. J., (2005) *IEEE Trans. Ultrason. Ferroelect. Freq. Control* **52** 2314 .

[14] Levi F., Shirley J. H., Heavner T. P., Yu D. and Jefferts S. R., (2006) *IEEE Trans. Ultrason. Ferroelect. Freq. Control* **53** 1584 .

[15] Shirley J. H., Levi F., Heavner T. P., Calonico D., Yu D .and Jefferts S. R., (2006) *IEEE Trans. Ultrason. Ferroelect. Freq. Control* **53** 2376 .

[16] Santarelli G. et al., (2009) *IEEE Trans. Ultrason. Ferroelect. Freq. Control* **56** 1319.

[17] Guena J., Li R. X., Gibble K., Bize S. and Clairon A., (2011) *Phys. Rev. Lett.* **106** 130801.

[18] Li R. X. and Gibble K., (2010) *Metrologia* **47** 534 .

[19] Levi F. et al., (2010) *IEEE Trans. Ultrason. Ferroelect. Freq. Control* **57** 600.

[20] Levi F., Lorini L., Calonico D. and Godone A., (2004) *IEEE Trans. Ultrason. Ferroelect. Freq. Control* **51** 1216 .

[21] Jefferts .S R., Drullinger R. E. and De Marchi A., (1998) *Proc. IEEE Symp. Freq. Control* 6 .

[22] Donley E. A., Heavner T. .P, Levi F., Tataw M. O. and Jefferts S. R., (2005) *Rev. Sci. Instrum.* **76** 063112 .

[23] Calosso C., Costanzo G. A. and De Marchi A., (2001) *Proceedings of 15th EFTF* 412.

[24] Bize S., Sortais Y., Mandache C., Clairon A. and Salomon C., (2001) *IEEE Trans. Instrum. Meas.* **50** 503.

[25] Jefferts S.R., Heavner T.P., Parker T.E.et al., (2013) *Phys. Rev. Lett*. Accepted for publication.

[26] Simon E. et al., (1998) Phys. Rev A 57, 436.

[27] Angstmann E.J., Dzuba V.A., Flanbaum V., (2006) *Phys. Rev. Lett*, 97 040801

[28] Calonico D., Cina A., Bendea I. H., Levi F., Lorini L. and Godone A., (2007) *Metrologia* **44** L44.

[29] Heavner T. P., Jefferts S. R., Donley E. A., Parker T. E. and Levi F., (2005) *Proc. Joint Meeting IEEE Intl. Freq. Control Symp. and PTTI* 308

[30] Guena J., Bize S., Clairon A., Li R. X. and Gibble K., (2010) *Proceedings of IEEE-Freq. Control Symposium* 307

[31] Weyers S., Geginov V., Nemitz N., Li R. X. and Gibble K., (2012) *Metrologia* **49** 82.

[32] Vanier J. and Audoin C., (1989) *The Quantum Physics of Atomic Frequency Standard* A. Hilger

[33] Godone A.., Micalizio S., Levi F. and Calosso C., (2006) *Phys. Rev. A* **74** 043401;

[34] Godone A., Micalizio S., Levi F. and Calosso C., (2011) *Review of Sc. Instr*

[35] Bauch A. *et al.*, (2006) Metrologia, **43**,109

[36] Dai-Hyuk Y., Weiss M. and Parker T. E, (2007) *Metrologia* **44** 91

[37] Panfilo G. and Parker T. E., (2007) *Proc. Joint Meeting. IEEE Intl. Freq. Control Symp. and EFTF Conf.* 805

[38] Parker T. E. and Panfilo G., (2007) *Proc. Joint Meeting. IEEE Intl. Freq. Control*

Symp. and EFTF Conf. 986

[39] ftp://ftp2.bipm.org/pub/tai/publication/cirt/